

Electronic Supplementary Information

The Fabrication of Three-Dimensional Plasmonic Chiral Structures by Glancing Angle Deposition

George K. Larsen,¹ Yizhuo He,¹ Whitney Ingram,¹ Ethan T. LaPaquette,¹ Jing Wang,² and Yiping Zhao¹

¹Department of Physics and Astronomy, and Nanoscale Science and Engineering Center, University of Georgia, Athens, GA 30602

²Department of Environment and Energy Resources
Beijing Institute of Technology, Haidian District Beijing, 100081 (China)

*Email: georgelarsen@physast.uga.edu; Phone: +1-706-542-6230; Fax: +1-706-542-2492

S1. Unpolarized UV-visible Spectra for the Ag/MgF₂ Helices, Stretched Chiral Patchy Particles, and HSPLs

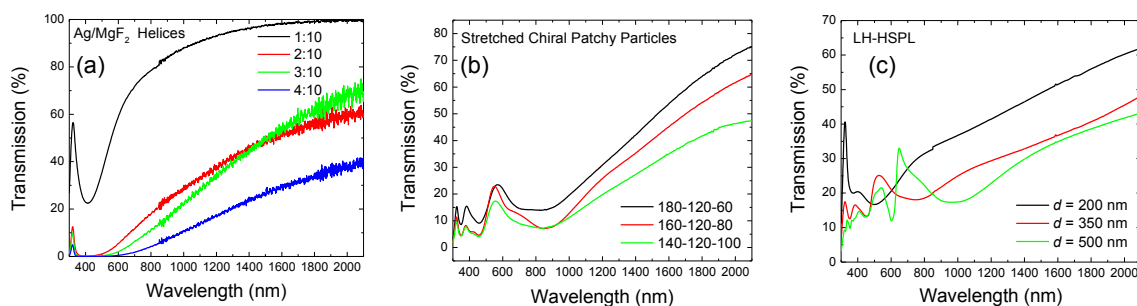


Figure S1. Unpolarized UV-vis transmission spectra for the (a) Ag/MgF₂ helices (b) stretched chiral patchy particles and (c) HSPL films.

S2. Point-Dipole Theory for Ag/MgF₂ Helices

In order to better understand the chiral optical properties of the Ag/MgF₂ helices, we have used the analytical point-dipole method developed by Fan and Govorov to calculate the circular dichroism response of helical chains of Ag nanoparticles embedded in a MgF₂ ambient.¹ In particular, we assume 20 spherical Ag nanoparticles of radius, a , are equally spaced in a helical arrangement of radius $r = 265$ nm, pitch $p = 800$ nm, and pitch number $N = 0.5$ (**Figure S2**). Here we have used variations in a to account for the

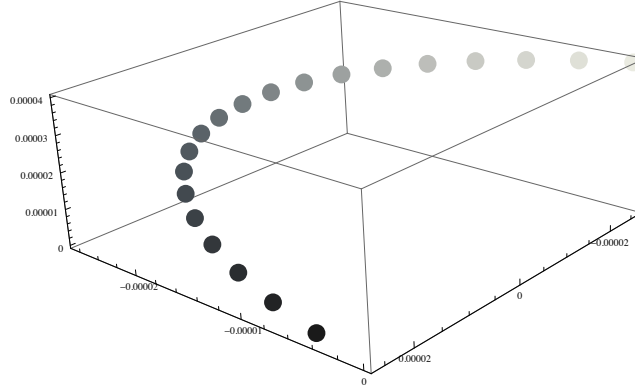


Figure S2. Plot of the Ag nanoparticle arrangement used in the point-dipole method calculations.

different volume ratios, where 1:10, 2:10, 3:10, and 4:10 have $a = 15.5, 19.5, 22.3,$ and 24.6 nm, respectively. These values were calculated assuming the Ag nanoparticles are embedded in MgF_2 helices with an arm diameter of 60 nm and a total length of 1100 nm. For the calculations, we also assume the ambient to have a refractive index of $n_0 = 1.38$ to match MgF_2 , and the Palik values were used for the Ag nanoparticles.²

Assuming a point dipole response from each individual Ag nanoparticle, the total electromagnetic field experienced by each nanoparticle is the external incident field plus the induced field from all other dipoles in the assembly. The problem of calculating the extinction of this entire assembly for different incident fields (e.g., right- and left-circular polarized light, LCP and RCP, respectively) can be solved self-consistently as described in the literature.^{1,3,4} Thus, using this analytical method we have calculated the circular dichroism, ϵ_{CD} , where $\epsilon_{\text{CD}} = \epsilon_{\text{LCP}} - \epsilon_{\text{RCP}}$ and ϵ_{LCP} and ϵ_{RCP} are the extinctions for LCP and RCP, respectively. The results of these calculations for the parameters given above are shown in **Figure S3a**. The calculated spectra differ slightly from the experimental spectra in that the films with greater Ag volume are theoretically predicted to have an increasingly higher CD response. Thus, for our experimental films, as the Ag volume

ratio increases, polarization-insensitive extinction also increases leading to a less than ideal CD response. Here, we describe this effect empirically by multiplying ϵ_{CD} by $\epsilon^{-\xi}$, where ϵ is the unpolarized extinction and ξ is an arbitrary exponential value. These results, which qualitatively agree with the experimental values, are plotted in **Figure S3b**.

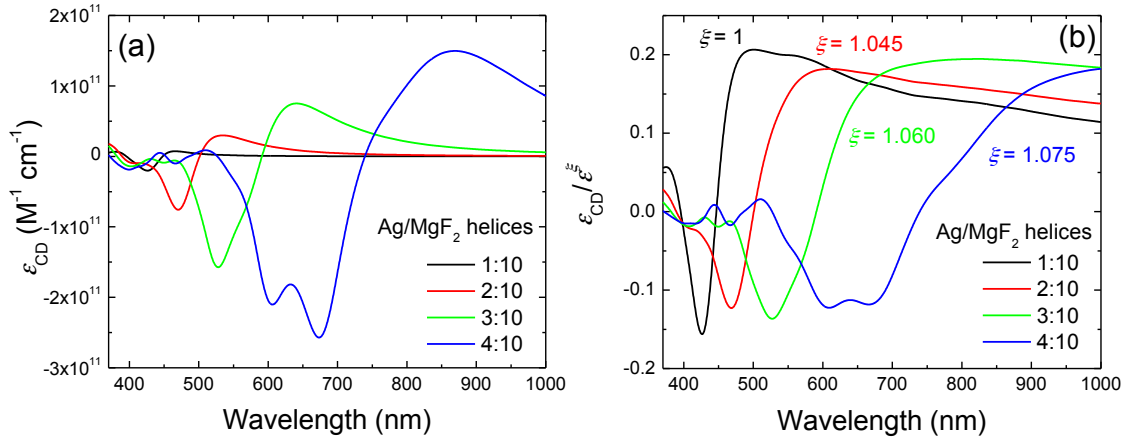


Figure S3. (a) Plot of the theoretical CD spectra for the Ag nanoparticle arrangement depicted in Fig. S2 for different Ag volume ratios. (b) Plot of the theoretical CD spectra normalized by the unpolarized extinction, ϵ , raised to the exponential value, ξ , given in the plot.

S3. Symmetry Breaking in Chiral Patchy Particles

As described in the manuscript, the shape of the Ag coating chiral patchy particle is determined by both the polar vapor incidence angle, θ , and the azimuthal orientation of the monolayer domain, φ , with respect to the vapor incidence (**Figure S4a**). Due to the 6-fold rotational symmetry of the hexagonal close packed (HCP) lattice of the monolayer domains, patch morphologies at φ_0 and $\varphi = \varphi_0 + j 60^\circ$ (where j is an integer and φ_0 is the initial orientation of the monolayer domain with respect to the vapor incidence) will be the same, and patch morphologies at φ_0 and $\varphi = j 60^\circ - \varphi_0$ will have the opposite handedness. Thus, depositing material at $\varphi = 0^\circ, 120^\circ$, and 240° should create a 3-fold rotationally symmetric patchy morphology. **Figure 4Sb** shows such simulated patchy

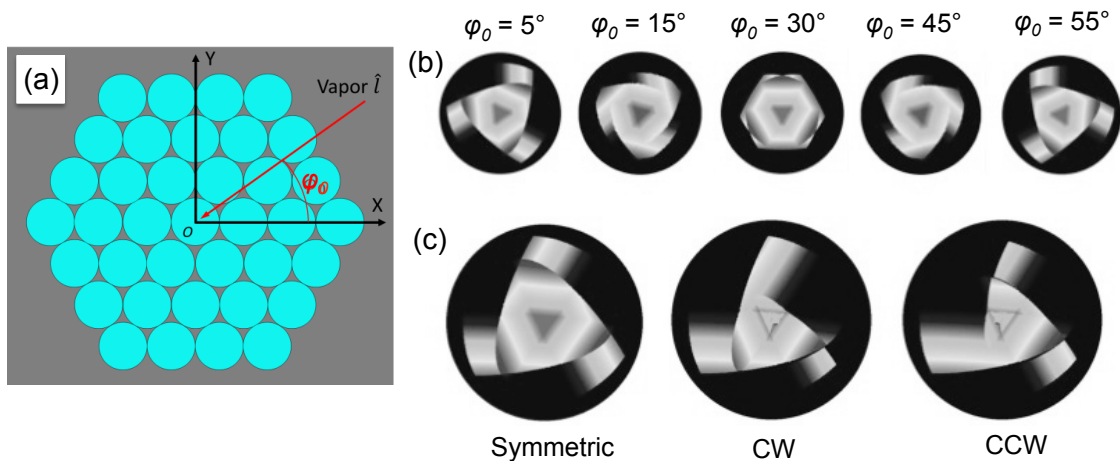


Figure S4. (a) Diagram of the hexagonal close packed lattice of the monolayer domains. (b) Diagrams showing the different simulated patch morphologies for various initial orientations, φ_0 , of the monolayer domain. (c) Simulated patchy morphology for $\varphi_0 = 55^\circ$ under the symmetric condition where the effects of material deposition are not included, and compares this with the patchy morphology where the effects of previously deposited material is included along with the effect of the different rotation directions, CW and CCW.

morphologies for various φ_0 orientations. However, the symmetry considerations above do not take into account the effect of previously deposited material, which when deposited sequentially over different azimuthal orientations, breaks the rotational symmetry of the HCP lattice. Furthermore, the rotational sense of the deposition (i.e., CCW: $\varphi = 0^\circ, 120^\circ, 240^\circ$ and CW: $\varphi = 0^\circ, 240^\circ, 120^\circ$) breaks this symmetry in opposite-handed ways. **Figure S4c** shows the simulated patchy morphology for $\varphi_0 = 55^\circ$ under the symmetry condition where the effects of material deposition are not included, and compares this with the patchy morphology where the effects of previously deposited material is included along with the effect of the different rotation directions, CW and CCW. Clearly, the CW and CCW patchy morphologies are significantly different from each other and from the symmetric condition. Importantly, the structural differences induced by the rotation direction enhance the chirality of patchy morphologies with a

specific handedness (i.e., $0^\circ < \varphi_0 < 30^\circ$ versus $30^\circ < \varphi_0 < 60^\circ$). This effect breaks the racemic symmetry of polycrystalline monolayer lattices, leading to an overall chiral optical response when using such substrates.⁵

S4. Materials and Methods

Ti/Ag helical films fabrication: The films are fabricated by a unique, custom designed vacuum deposition system equipped with two electron-beam evaporation sources (co-deposition system, Pascal Technology). The source materials used are Ti (99.9 %, Kurt J. Lesker) and Ag (99.995 %, Kurt J. Lesker). Prior to the deposition, the vacuum chamber is evacuated to a pressure of 1×10^{-6} Torr, and the background pressure during the deposition is maintained at less than 5×10^{-6} Torr. Pre-cleaned quartz slides and Si wafers are used as substrates, and are chosen for different characterizations. The substrate normal is positioned at $\theta = 87^\circ$ with respect to the vapor incident direction, and the azimuthal rotation rates are set to 0.038 rpm, 0.005 rpm, and 0.0025 rpm for STF1, STF2, and STF3, respectively. The Ti/Ag ratio is controlled by the relative growth rates of Ti (0.01 nm/s) and Ag (0.19 nm/s), which are monitored independently by two separate quartz crystal microbalances (QCMs). The deposition proceeds until the total thickness from both QCMs reach 1 μm .

Ag/MgF₂ helical films fabrication: The films are fabricated by the above mentioned co-deposition system. The source materials used are MgF₂ (99.9 %, Kurt J. Lesker) and Ag (99.995 %, Kurt J. Lesker). The substrate normal is positioned at $\theta = 87^\circ$ with respect to the vapor incident direction, and the azimuthal rotation rate is set to 0.1 rpm for the structure seen in Figure 2a in the main manuscript and 0.0007 rpm for the structures in

Figure 2b. The Ag:MgF₂ volume ratios are controlled by the relative growth rates. The total deposition thicknesses (Ag + MgF₂) are 2000 nm and 1000 nm for the structures in Figure 2a and Figure 2b, respectively.

Self-assembled colloid monolayer (SACM) preparation: Colloid monolayers are formed using an air/water interface technique using polystyrene (PS) bead solutions (Polyscience, 2.6 wt%) containing beads of different diameters, $d = 200, 350, 500, 750,$ and 2000 nm. First, the PS bead solutions are washed using ultra-pure (18 M Ω) water by centrifugation and then diluted with ultra-pure water to concentrations ranging between 0.6 to 0.24 wt%. After ultra-sonication for 30 minutes, the solution is further diluted by adding a 2:1 ratio of bead solution and ethanol. Next, a cleaned petri dish, tilted at a 3° angle from a flat surface, is filled with a shallow layer of ultra-pure water. In order to control the flow of the prepared PS solutions into the petri dish, a syringe (Monoject) with a 90° bent needle is attached to a syringe pump (KD Scientific). The tip of the needle is positioned close, but not touching the water surface, and PS solution droplets are dispensed onto the water's surface at rates ranging between 0.008 to 0.015 mL/min. The dispersion of the beads on the water surface forms well-ordered monolayers over time. After the monolayer is completely formed, the water level is slowly raised, and a Teflon ring is placed on the surface of the water to confine the monolayer. Ultra-pure water is simultaneously pumped in by the syringe pump and removed using a multi-staltic water pump (Buchler Instruments) to remove any residual sunken beads. Then, pre-cleaned Si and glass substrates are carefully placed underneath the monolayer by sliding them to the area below the Teflon ring using tweezers. Lastly, the syringe pump

slowly removes all water allowing the confined monolayer to deposit on the surface of the underlying substrates.

Chiral patchy film deposition: The patchy films are fabricated in the co-deposition system. Ag pellets are used as source materials (Plasma Materials, 99.99%). The SACM substrates are loaded onto the GLAD substrate holder, which is positioned such that the substrate normal forms an $\theta = 86^\circ$ angle with respect to the vapor incident direction. The chamber is evacuated to 1×10^{-6} Torr, and is maintained at a pressure of $< 5 \times 10^{-6}$ Torr throughout the deposition. The Ag evaporation rate (0.05 nm/s) and thickness are monitored by a QCM. Material is deposited in 30 nm increments at each azimuthal rotation angle until the final desired QCM thickness of 120 nm at each angle is achieved. The clockwise (CW) and counter-clockwise (CCW) films are rotated azimuthally in -120° and 120° increments, respectively.

Stretched chiral patchy films: The stretched chiral patchy films are prepared similar to the chiral patchy films above, except that material is deposited in different incremental amounts at each azimuthal angle. For example, for the 180-120-60 film, material is deposited in 45 nm, 30 nm, and 15 nm increments at 0° , 120° , and 240° , respectively, through four cycles.

Oligomer films: SACMs and source materials are loaded into the co-deposition chamber as described above. As shown in Figure 5a in the main manuscript, first 15 nm of MgF_2 is deposited at vapor incident angle $\theta = 0^\circ$. Then, the substrate is repositioned such that the vapor incident angle is $\theta = 86^\circ$, and 80 nm of Ag is deposited. Next, the substrate is rotated azimuthally by $\varphi = 90^\circ$, and the MgF_2 and Ag depositions are again repeated

using $\theta = 0^\circ$ and $\theta = 86^\circ$, respectively. The substrate is then rotated azimuthally by another $\varphi = 90^\circ$, and the MgF_2 and Ag depositions are repeated once more. A final MgF_2 deposition at $\theta = 0^\circ$ finishes the process.

Helically stacked plasmonic layers: SACMs and source materials, Ag (99.999%, Kurt J. Lesker) and SiO_2 (99.99%, International Advanced Materials), are loaded into the co-deposition chamber. If we define $\Delta\varphi$ as the relative change in azimuthal orientation of the substrates with respect to the previous step, and denote + and - for counterclockwise and clockwise rotations, respectively, then the sequence of depositions for right-hand HSPLs (left-hand HSPLs) can be described by: (1) Ag: $\Delta\varphi = 0^\circ$, (2) SiO_2 : $\Delta\varphi = 180^\circ$, (3) Ag: $\Delta\varphi = -90^\circ$ (90°), (4) SiO_2 : $\Delta\varphi = 180^\circ$, (5) Ag: $\Delta\varphi = -90^\circ$ (90°), (6) SiO_2 : $\Delta\varphi = 180^\circ$, and (7) Ag: $\Delta\varphi = -90^\circ$ (90°), where each Ag or SiO_2 layer has a nominal thickness of 30 nm (see Figure 6a in the main manuscript for a schematic of the deposition process). The deposition rate for both Ag and SiO_2 is maintained at 0.05 nm/s throughout the deposition, as monitored by a QCM. The deposition of Ag or SiO_2 for each layer continued until a final QCM thickness of 30 nm is reached.

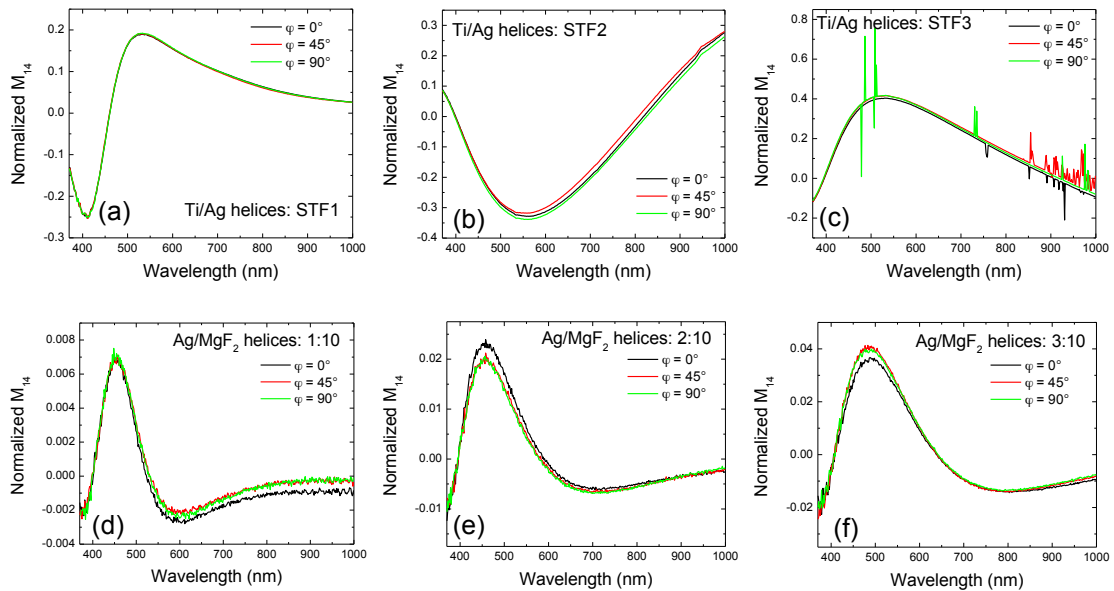
Morphological Characterization: The scanning electron microscope (SEM) images of the different structures and films are collected using a field-emission scanning electron microscope (FEI Inspect F). The transmission electron microscope (TEM) images of individual particles are collected using a transmission electron microscope (Tecnai 20).

Optical Characterization: A variable angle spectroscopic ellipsometer (M-2000, J. A. Woollam, Inc.) is used in transmission mode to measure the first three rows of the Mueller matrix describing the sample with the $m_{11}(\lambda)$ element normalized to 1. The

unpolarized transmission is measured by UV-visible spectrophotometer (JASCO V-570) and used to measure the un-normalized $M_{11}(\lambda)$ Mueller matrix element. The un-normalized $m_{11}(\lambda)$ and $M_{14}(\lambda)$ elements are used to determine $\Delta T = T_{\text{LCP}} - T_{\text{RCP}}$, where T_{LCP} and T_{RCP} are the transmission percentages for LCP and RCP, respectively. In particular, $\Delta T(\lambda) = -2 M_{14}(\lambda)$. The Mueller matrix is measured and averaged over several azimuthal orientations, $\varphi = 0^\circ, 45^\circ,$ and 90° , to account for linear effects (See Section S3 for all of the spectra).^{6,7}

S5. Raw Ellipsometry Data

The figures below show the azimuthal ellipsometry measurements that were averaged over to obtain the $\Delta T = T_{\text{LCP}} - T_{\text{RCP}}$ spectra for all samples described in the manuscript. The very last figure compares the raw $M_{14}(\lambda)$ spectra for air, a dielectric MgF_2 helix, and the plasmonic Ag/MgF_2 helices to demonstrate that the weak signal from these films is within the measurement resolution of the ellipsometer.



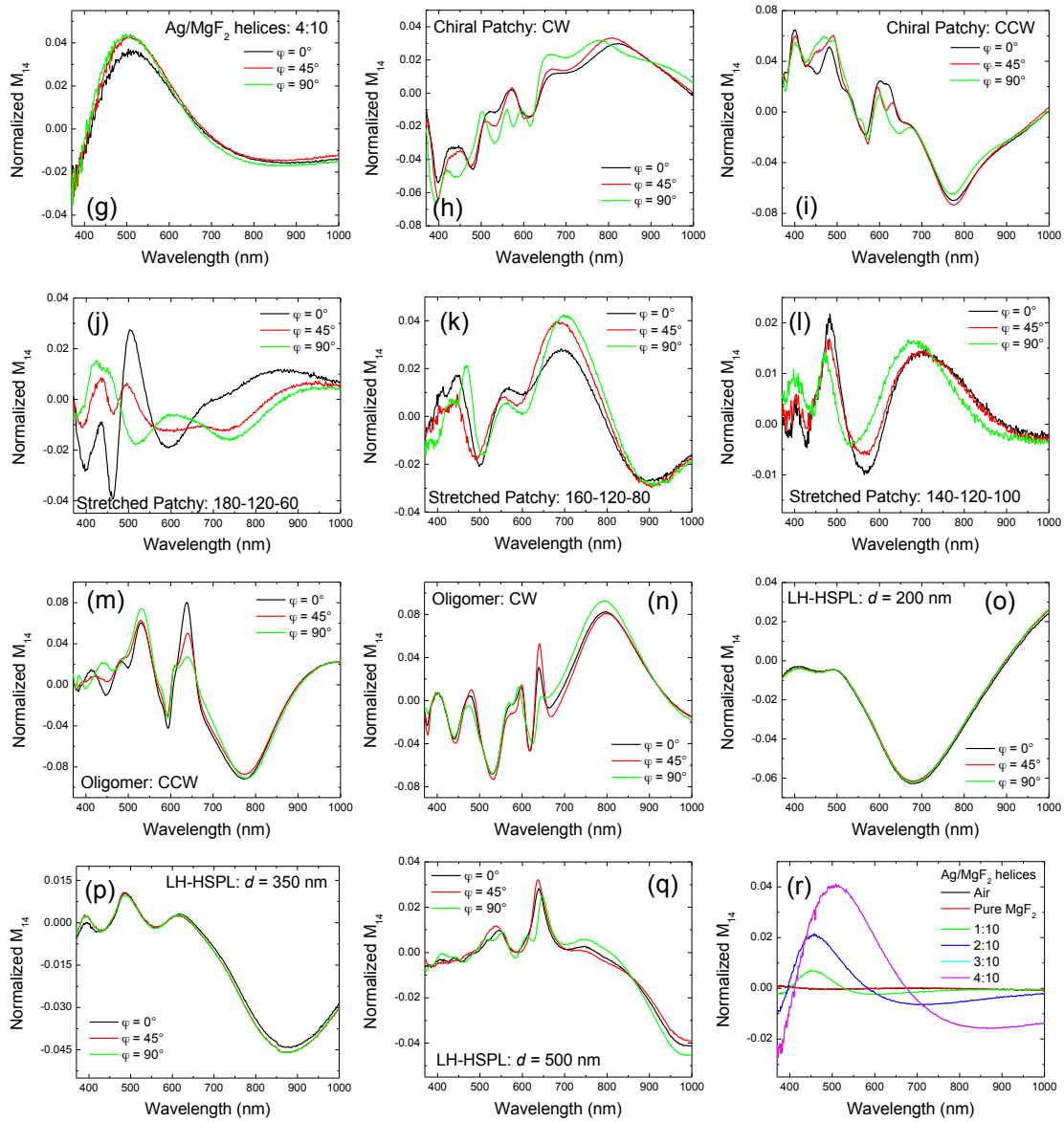


Figure S5. Raw data from the ellipsometer, in the form of the normalized M_{14} Mueller matrix element, as a function of azimuthal angle, φ , for Ti/Ag helices (a) STF1, (b) STF2, and (c) STF3; (d) – (g) Ag/MgF₂ helices with compositions 1:10, 2:10, 3:10, and 4:10, respectively; (h) CW and (i) CCW chiral patchy particles; (j) 180-120-60, (k) 160-120-80, and (l) 140-120-100 stretched chiral patchy particles; (m) CCW and (n) CW oligomers; (o) – (q) LH-HSPLs on $d = 200, 350,$ and 500 nm colloidal bead substrates, respectively. (r) Comparison of the raw data from the ellipsometer for air, a dielectric MgF₂ helix with the same parameters (e.g., pitch, radius, etc.) as the Ag composite structures, and the Ag/MgF₂ helices at the various compositions.

S6. References

1. Z. Fan and A. O. Govorov, *Nano Lett.*, 2010, **10**, 2580-2587.
2. E. D. Palik, *Handbook of optical constants of solids*, Academic press, 1998.
3. A. Kuzyk, R. Schreiber, Z. Fan, G. Pardatscher, E.-M. Roller, A. Hogele, F. C. Simmel, A. O. Govorov and T. Liedl, *Nature*, 2012, **483**, 311-314.
4. J. H. Singh, G. Nair, A. Ghosh and A. Ghosh, *Nanoscale*, 2013, **5**, 7224-7228.
5. G. Larsen, Y. He, W. Ingram and Y. Zhao, *Nano Lett.*, 2013, **13**, 6228–6232.
6. E. Castiglioni, P. Biscarini and S. Abbate, *Chirality*, 2009, **21**, E28-E36.
7. J. Schellman and H. P. Jensen, *Chemical Reviews*, 1987, **87**, 1359-1399.